

# Impact of Sr Addition on Zirconia–Alumina-Supported Ni Catalyst for CO<sub>x</sub>-Free CH<sub>4</sub> Production via CO<sub>2</sub> Methanation

Abdulaziz A. M. Abahussain, Ahmed S. Al-Fatesh,\* Yuvrajsinh B. Rajput, Ahmed I. Osman,\* Salwa B. Alreshaidan, Hamid Ahmed, Anis H. Fakeeha, Abdulrhman S. Al-Awadi, Radwa A. El-Salamony, and Rawesh Kumar\*



Cite This: *ACS Omega* 2024, 9, 9309–9320



Read Online

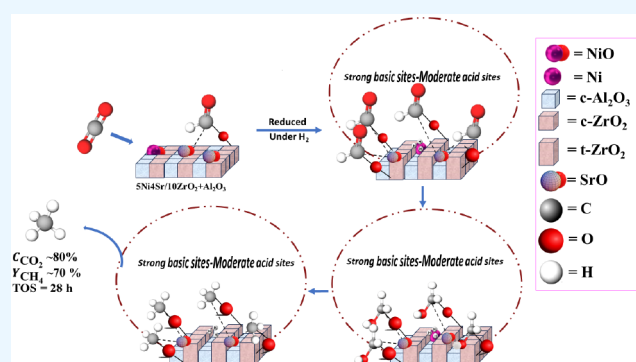
ACCESS |

Metrics & More

Article Recommendations

Supporting Information

**ABSTRACT:** Zirconia-alumina-supported Ni (5Ni/10ZrO<sub>2</sub>+Al<sub>2</sub>O<sub>3</sub>) and Sr-promoted 5Ni/10ZrO<sub>2</sub>+Al<sub>2</sub>O<sub>3</sub> are prepared, tested for carbon dioxide (CO<sub>2</sub>) methanation at 400 °C, and characterized by X-ray diffraction, X-ray photoelectron spectroscopy, surface area and porosity, infrared spectroscopy, and temperature-programmed reduction/desorption techniques. The CO<sub>2</sub> methanation is found to depend on the dispersion of Nickel (Ni) sites as well as the extent of stabilization of CO<sub>2</sub>-interacted species. The Ni active sites are mainly derived from the reduction of ‘moderately interacted NiO species’. The dispersion of Ni over 1 wt % Sr-promoted 5Ni/10ZrO<sub>2</sub>+Al<sub>2</sub>O<sub>3</sub> is 1.38 times that of the unpromoted catalyst, and it attains 72.5% CO<sub>2</sub> conversion (against 65% over the unpromoted catalyst). However, increasing strontium (Sr) loading to 2 wt % does not affect the Ni dispersion much, but the concentration of strong basic sites is increased, which achieves 80.6% CO<sub>2</sub> conversion. The 5Ni4Sr/10ZrO<sub>2</sub>+Al<sub>2</sub>O<sub>3</sub> catalyst has the highest density of strong basic sites and the highest concentration of active sites with maximum Ni dispersion. This catalyst displays exceptional performance and achieves approximately 80% CO<sub>2</sub> conversion and 70% methane (CH<sub>4</sub>) yield for up to 25 h on steam. The unique acidic–basic profiles composed of strong basic and moderate acid sites facilitate the sequential hydrogenation of formate species in the CO<sub>x</sub>-free CH<sub>4</sub> route.



## 1. INTRODUCTION

The catalytic conversion of CO<sub>2</sub> to CH<sub>4</sub> represents a promising approach to reducing CO<sub>2</sub> concentration in the environment and addressing the energy crisis through CH<sub>4</sub> production.<sup>1</sup> CH<sub>4</sub> can serve as a substitute for natural gas,<sup>2</sup> and it can also be used to generate electricity.<sup>3</sup> CO<sub>2</sub> methanation is a crucial process for future space travel as its reactants, CO<sub>2</sub> and H<sub>2</sub>, are continuously produced from respiration and water electrolysis.<sup>4</sup> The production of H<sub>2</sub> from electrolysis and then the potential conversion of H<sub>2</sub> and CO<sub>2</sub> into methane is termed as the power-to-gas conversion process.<sup>5</sup>

This reaction is commonly termed as the CO<sub>2</sub> methanation reaction. From a catalytic perspective, there is a preference for cost-effective Ni-based catalysts over precious metals, such as Ru, Ir, Rh, and Pd for methanation reactions.<sup>3,6,7</sup> These Ni-based catalysts offer a more economical and sustainable solution for efficient CO<sub>2</sub> conversion into CH<sub>4</sub>, making them a key focus in current research and development efforts.<sup>8</sup> The interaction between CO<sub>2</sub> and the catalyst site is influenced by two critical factors: surface basicity and reducibility. Surface basicity induces the CO<sub>2</sub> interaction. Metallic Ni and oxygen defects are formed as a consequence of surface reduction.

Oxygen defects are the sites where CO<sub>2</sub> activation occurs, while metallic Ni facilitates H<sub>2</sub> dissociation.<sup>9</sup> The interaction between activated CO<sub>2</sub> and dissociated hydrogen molecules progresses the CO<sub>2</sub> hydrogenation reaction through two routes: the direct route, which does not involve CO as an intermediate, and the indirect route, which includes CO as an intermediate in the reaction mechanism. For instance, a zirconia-supported Ni catalyst prepared by the plasma decomposition method exhibits more exposed Ni (111) sites (for H<sub>2</sub> dissociation) with fewer defects.<sup>10</sup> Indeed, the presence of fewer defects might not be sufficient to adequately stabilize the formate species, leading to its further decomposition into CO, which is subsequently hydrogenated into CH<sub>4</sub> through an indirect route. Zirconia-supported Ni catalysts prepared through the thermal decomposition method

**Received:** October 28, 2023

**Revised:** January 27, 2024

**Accepted:** February 2, 2024

**Published:** February 14, 2024



introduce a suitable number of defects, thereby ensuring the effective stabilization of formate species. Consequently, this facilitates the sequential hydrogenation of formate into CH<sub>4</sub> (without the formation of CO) through a direct route. This emphasizes the influence of catalyst preparation methods on the reaction mechanism in the CO<sub>2</sub> methanation reaction.

Zirconia has oxygen-endowing capacity and yttria-zirconia has thermal stability as well.<sup>10</sup> Notably, zirconia-supported Ni catalysts, Sr-modified Ni-ZrO<sub>2</sub>, and lanthana-zirconia-supported Ni catalysts have been recognized for achieving 100% CH<sub>4</sub> selectivity through the direct methanation route.<sup>11–13</sup> In alumina-zirconia-supported Ni catalysts (Al/Zr = 1/10 molar ratio), the H<sub>2</sub> dissociation capacity over Ni was enhanced.<sup>14</sup> In the same way, enhanced basicity was observed over Sr-doped Ni-based catalysts supported over the WO<sub>3</sub>+ZrO<sub>2</sub> catalyst, which showed 90% CO<sub>2</sub> conversion and 84% CH<sub>4</sub> yield up to 300 min at 350 °C.<sup>14,15</sup> Considering the catalyst cost, the cheap alumina and silica supports have consistently garnered significant interest compared to other supports, such as yttria, zirconia, lanthana, and ceria. Among the alumina and silica, silica has a lower Ni dispersion ability, which caused inferior catalytic activity toward the CO<sub>2</sub> methanation reaction.<sup>16</sup> The utilization of 20 wt % Ni supported over Al<sub>2</sub>O<sub>3</sub> resulted in 75% CO<sub>2</sub> conversion and 96% CH<sub>4</sub> selectivity.<sup>17,18</sup> However, in the case of an alumina-supported Ni catalyst, Ni tends to migrate into the alumina lattice, thereby affecting both hydrogen dissociation and hydrogenation of CO<sub>2</sub>. To mitigate this issue, the incorporation of ZrO<sub>2</sub> alongside alumina prevents the diffusion of Ni into the alumina lattice, resulting in improved stability in the CO<sub>2</sub> methanation reaction.<sup>19</sup> Moreover, the addition of ZrO<sub>2</sub> into the Ni–Al binary hydrotalcite was found to increase the number of basic sites as well as surface oxygen vacancy.<sup>20</sup> Ni-based nanocatalysts with 15 wt % Zr contents prepared from NiZrAl-layered double hydroxide precursors were observed to enrich the catalyst surface with ‘Zr<sup>3+</sup>–oxygen vacancy’ species, which are crucial for CO<sub>2</sub> activation.<sup>21</sup> The addition of silica to alumina in Ni-based catalysts shows inferior catalytic performance in the CO<sub>2</sub> methanation reaction.<sup>22</sup> However, when Si/Al = 0.5, the Ni/Al<sub>2</sub>O<sub>3</sub>–SiO<sub>2</sub> catalyst exhibited improved reducibility and high dispersion of metallic Ni. This favorable configuration resulted in notable performance, achieving an 82.38% CO<sub>2</sub> conversion and 98.19% CH<sub>4</sub> selectivity at 350 °C.<sup>23</sup> The presence of 15 wt % MnO<sub>2</sub> in 10 wt % NiO–Al<sub>2</sub>O<sub>3</sub> catalyst caused enhanced reducibility, higher CO<sub>2</sub> adsorption, enhanced dispersion of active sites, and stable catalytic activity (84% CO<sub>2</sub> conversion and 98% CH<sub>4</sub> selectivity) up to 800 min.<sup>24</sup> The incorporation of 10 wt % Co into Al<sub>2</sub>O<sub>3</sub>-supported 10 wt % Ni catalyst had a positive impact, enhancing both Ni dispersion and reducibility, which turned into an improved performance of >65% CO<sub>2</sub> conversion (as compared to the 60% CO<sub>2</sub> conversion over 10Ni/Al<sub>2</sub>O<sub>3</sub>) and 95% CH<sub>4</sub> selectivity at 350 °C.<sup>17</sup> Using CaO along with Al<sub>2</sub>O<sub>3</sub> (Ca/Al = 1/2 mol ratio) as support for Ni-based catalysts was found to enhance the reducibility and activity (~80% CO<sub>2</sub> conversion and 99% CH<sub>4</sub> selectivity) for up to 12 h.<sup>25</sup> 3 wt % Co-promotional addition over 10 wt % Ni supported on CaO–Al<sub>2</sub>O<sub>3</sub> (Ca/Al = 1/2) further induced a higher degree of reducibility and formation of more active sites, which resulted in 83% CO<sub>2</sub> conversion and 99% CH<sub>4</sub> selectivity constantly up to 900 min.<sup>26</sup> Introducing 5 wt % Fe into 30 wt % Ni/Al<sub>2</sub>O<sub>3</sub> resulted in improved reducibility, significantly enhancing CO<sub>2</sub> conversion, reaching approximately 70% CO<sub>2</sub> conversion (~99% CH<sub>4</sub> selectivity) at 35

°C.<sup>27</sup> The addition of lanthana to the Ni/Al<sub>2</sub>O<sub>3</sub> catalyst introduced moderate basic sites and significantly improved both Ni dispersion and reducibility.<sup>28</sup> The interface between LaO<sub>x</sub> and Ni crystallite may be accountable for catalytic activity toward CO<sub>2</sub> methanation.<sup>29</sup> The incorporation of lanthana into silica-modified alumina enhances the catalyst's basicity, leading to a significant improvement in CH<sub>4</sub> selectivity, with almost 100% CH<sub>4</sub> selectivity (84% CH<sub>4</sub> yield) achieved at a reaction temperature of 300 °C.<sup>19</sup> The stoichiometric ratio of MgO, NiO, and Al<sub>2</sub>O<sub>3</sub> in hydrotalcite-like structures led to a strong interaction of NiO with the hydrotalcite matrix, resulting in catalytic inferiority. However, with an increase in Ni loading to 42.5 wt % in hydrotalcite, the interaction of NiO with the matrix weakened, leading to higher catalytic activity with 82% CO<sub>2</sub> conversion and 99% CH<sub>4</sub> selectivity achieved at 300 °C. Furthermore, the addition of yttria to the alumina-supported Ni catalyst was found to enhance reducibility, increase CO<sub>2</sub> uptake, and improve the interaction between Ni and the Al<sub>2</sub>O<sub>3</sub> support.<sup>30</sup> Sr incorporation in Ni/Al<sub>2</sub>O<sub>3</sub> optimizes the crystalline size.<sup>31</sup> It was observed that alumina-supported SrO exhibits higher CO<sub>2</sub>-carrying capacity compared to unsupported SrO, which makes promising material for CO<sub>2</sub> capture and catalysis.<sup>15,31–33</sup> The incorporation of Sr into alumina-supported Rh–Mn catalyst has been observed to impact the degree of reduction and CO chemisorption, leading to enhanced CO<sub>2</sub> conversion (73%) and 40% CH<sub>4</sub> yield at 210 °C.<sup>34</sup> Moreover, the use of zirconia-based support has been found to provide resistance to the sintering of SrO during CO<sub>2</sub> sorption at high temperatures.<sup>35</sup>

After an extensive literature survey, we speculate that the strontium-promoted alumina-supported Ni catalyst may be excellent for the CO<sub>2</sub> methanation reaction. But it may encounter sintering of SrO at high temperatures and diffusion of Ni into the alumina lattice.<sup>19,32,35</sup> Using zirconia proportion along with alumina can provide resistance to SrO sintering, and it can prevent the diffusion of Ni into alumina lattice. In this study, we have developed a novel strontium-promoted zirconia-alumina-supported Ni catalyst for CO<sub>2</sub> methanation. Prior to the reaction, the catalyst underwent reduction, and various characterizations, including X-ray diffraction, surface area and porosity analysis, CO<sub>2</sub>-temperature-programmed reduction, infrared spectroscopy, and transmission electron microscopy, were conducted to assess its properties. The fresh catalysts were also characterized and discussed for comparison purposes. XPS analysis provided valuable insights into the oxidation states of the elements within the catalyst. By closely correlating the characterization results with catalytic activity, we aim to establish a well-suited catalyst for industrial CO<sub>2</sub> methanation in the near future. The findings of this study pave the way for the development of efficient and sustainable catalysts to address the challenges of CO<sub>2</sub> methanation.

## 2. EXPERIMENTAL SECTION

**2.1. Material.** Ni (NO<sub>3</sub>)<sub>2</sub>·6H<sub>2</sub>O (Fisher, Germany), Sr (NO<sub>3</sub>)<sub>2</sub>·6H<sub>2</sub>O (Fisher, Germany), and 10ZrO<sub>2</sub>+γ-Al<sub>2</sub>O<sub>3</sub> microspheres (dp = 400–500 μm; Daiichi Kigenso Kagaku Kogyo Co., Ltd.) were used to prepare the catalysts. As per the specification of 10ZrO<sub>2</sub>+Al<sub>2</sub>O<sub>3</sub> (from Daiichi Kigenso Kagaku Kogyo Co., Ltd.), the 10ZrO<sub>2</sub>+Al<sub>2</sub>O<sub>3</sub> support has 126 m<sup>2</sup>/g surface area and 50% of particles in the catalyst are smaller than 60.3 μm (D<sub>50</sub> = 60.3 μm). It has tetragonal ZrO<sub>2</sub> and cubic γ-Al<sub>2</sub>O<sub>3</sub> phases. The concentration of basic sites and acidic sites over the 10ZrO<sub>2</sub>+Al<sub>2</sub>O<sub>3</sub> support is lower than ZrO<sub>2</sub>.

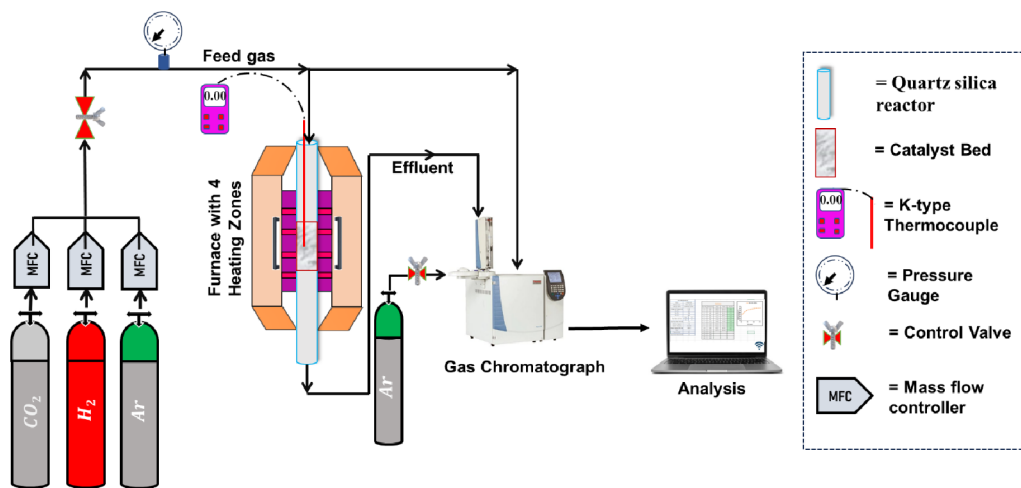


**Figure 1.** Systematic diagram for experimental setup for the CO<sub>2</sub> methanation reaction.

**2.2. Catalyst Preparation.** 5 wt % nickel and 1–4 wt % strontium are incorporated into 10ZrO<sub>2</sub>+γ-Al<sub>2</sub>O<sub>3</sub> by an impregnation method. Nickel nitrate (equivalent to 5 wt % Ni) and strontium nitrate solutions (equivalent to 1–4 wt %) are added to the 10ZrO<sub>2</sub>+γ-Al<sub>2</sub>O<sub>3</sub> support while stirring and heating. The mixture is held in an 80 °C bath with moderate stirring until it evaporates. It is then dried overnight at 110 °C before being calcined for 30 min at 450 °C (heating ramp 1 °C/min). The prepared catalysts are named as 5Ni/10ZrO<sub>2</sub>+Al<sub>2</sub>O<sub>3</sub>, 5Ni1Sr/10ZrO<sub>2</sub>+Al<sub>2</sub>O<sub>3</sub>, 5Ni2Sr/10ZrO<sub>2</sub>+Al<sub>2</sub>O<sub>3</sub>, 5Ni3Sr/10ZrO<sub>2</sub>+Al<sub>2</sub>O<sub>3</sub>, and 5Ni4Sr/10ZrO<sub>2</sub>+Al<sub>2</sub>O<sub>3</sub>.

**2.3. Catalysts Characterization.** The X-ray diffraction study of the catalyst sample is carried out with a Miniflex Rigaku diffractometer (Rigaku, Saudi Arabia) using a Cu<sub>Kα</sub> source (λ = 1.54056) operated at 40 kV and 40 mA. The step size and scanning range of 2θ for analysis were set to 0.01 and 5–100, respectively. The peak search profile is adjusted at a minimum significance of 2, minimum tip width of 2θ = 0.01°, maximum tip width 2θ = 1°, and peak base width of 2° under the minimum second derivative method. Peak search and matching are carried out at a search depth of 10 and a minimum scale factor of 0.1. The diffraction patterns of the sample are matched with the JCPDS database for phase analysis. The oxidation state of elements is determined by X-ray photoelectron spectroscopy (XPS) using a Thermo-fisher Scientific instrument (USA) through an Al<sub>Kα</sub> excitation source and 20 eV pass energy. The N<sub>2</sub> adsorption–desorption profile against relative pressure (P/P<sub>o</sub>), surface area, pore volume, and pore diameter of the catalyst sample was obtained from Micromeritics Tristar II 3020 instrument (Micromatics, USA). The surface area is estimated by the Brunauer–Emmet–Teller equation, whereas pore size distribution is estimated by the nonlocal density function model. The reducibility, basicity, and acidity profiles are studied by H<sub>2</sub>-temperature-programmed reduction (H<sub>2</sub>-TPR), CO<sub>2</sub>-temperature-programmed desorption and NH<sub>3</sub>-temperature-programmed desorption by using Micromeritics Autochem II 2920 (Micromatics, USA) and thermal conductivity detector (TCD). For H<sub>2</sub>-TPR, 70 mg of the sample was heated to 900 °C (at a heating ramp of 10 °C/min) under 10% H<sub>2</sub>/Ar gas feed (flow rate 40 mL/min). After the interaction of the gas feed with a surface, H<sub>2</sub>O is formed, which is removed using a cold trap. The Ni dispersion was evaluated by a H<sub>2</sub> chemisorption study using a BELCAT II

Catalyst Analyzer. After in situ reduction of the sample at 700 °C for 1 h in 5% H<sub>2</sub>–N<sub>2</sub> mixture (30 mL/min), it was cooled down in the inert atmosphere to 100 °C, and pulses of 5% H<sub>2</sub>–N<sub>2</sub> mixture of known volume were injected until the metal surface was saturated and no further H<sub>2</sub> uptake was observed. For TPD, 70 mg of the sample was cleaned using helium flow at 200 °C for 1 h. Then, it was fed with a mixture of 10% CO<sub>2</sub> (or 10% NH<sub>3</sub>)/He gas feed (flow rate 30 mL/min) at 50 °C for 30 min. CO<sub>2</sub> or NH<sub>3</sub> was desorbed with an increasing temperature of up to 900 °C. The change in conductivity due to the consumption of H<sub>2</sub> in TPR or desorption of gases in TPD over the catalyst surface was recorded by a temperature conductivity detector (TCD). Fourier transform infrared (FTIR) spectra of catalyst samples were taken by Prestige-21 SHIMADZU. The catalyst morphology was observed by 120 kV JEOL JEM-2100F (Akishima, Japan) transmission electron microscope (TEM).

**2.4. Catalytic Activity Test.** The reactor set for the CO<sub>2</sub> methanation reaction is shown in Figure 1. The CO<sub>2</sub> methanation reaction is carried out over a packed catalyst (2 g of catalyst diluted with silicon carbide up to 5 cm bed height) in a tubular fixed bed quartz silica reactor (length = 50 cm, inner diameter = 13 mm, catalyst bed volume 5 cm<sup>3</sup>). The temperature for the reaction is given by a peripheral programmable electric furnace, and the temperature of the catalyst bed is monitored by a K-type thermocouple, which is placed axially in the middle of the catalyst bed (as shown in Figure 1). First, the catalyst is reduced under H<sub>2</sub> (flow rate 30 mL/min) for 2 h at 700 °C, and then the reactor is cooled down. Furthermore, for the methanation reaction, CO<sub>2</sub>: H<sub>2</sub>: Ar (1:4:5 volume ratio) gas feed is passed over the reduced catalyst at 6000 ccg<sup>-1</sup>h<sup>-1</sup> GHSV and a 400 °C reaction temperature. The reaction products and unconverted feed gases from the reactor were evaluated quantitatively by using an online GC (GC-Shimadzu 2014) equipped with molecular sieve 5A and Porapak Q column and thermal conductivity detector (TCD). The carbon dioxide conversion ( $X_{\text{CO}_2}$ ) and methane yield ( $Y_{\text{CH}_4}$ ) are calculated as shown below:<sup>19</sup>

$$X_{\text{CO}_2}(\%) = \frac{\text{CO}_{2,\text{in}} - \text{CO}_{2,\text{out}}}{\text{CO}_{2,\text{in}}} \times 100 \quad (1)$$

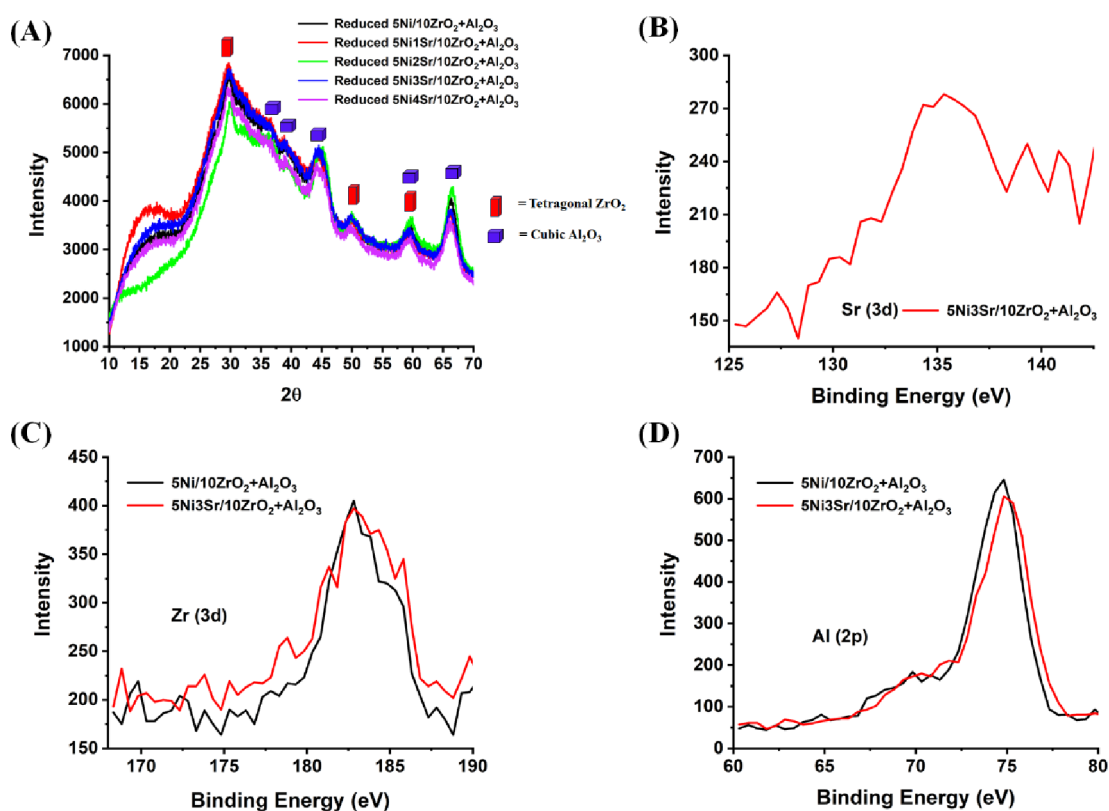


**Figure 2.** (A) X-ray diffraction patterns of the reduced Ni/10ZrO<sub>2</sub>+Al<sub>2</sub>O<sub>3</sub> and reduced Ni<sub>x</sub>Sr/10ZrO<sub>2</sub>+Al<sub>2</sub>O<sub>3</sub> ( $x = 1-4$ ) catalyst system. (B) Sr (3d) XPS spectra, (C) Zr (3d) XPS spectra, and (D) Al (2p) XPS spectra.

$$Y_{\text{CH}_4}(\%) = \frac{\text{CH}_{4,\text{out}}}{\text{CO}_{2,\text{in}}} \times 100 \quad (2)$$

### 3. RESULTS AND DISCUSSION

**3.1. Characterization Results.** Before the onset of the CO<sub>2</sub> methanation reaction, catalyst reduction was performed. Hence, identifying phase distribution, surface area, basicity, and acidity profiles over the reduced catalyst system is essential herein. Figure 2A displays the X-ray diffraction results for the reduced Ni/10ZrO<sub>2</sub>+Al<sub>2</sub>O<sub>3</sub> and reduced Ni<sub>x</sub>Sr/10ZrO<sub>2</sub>+Al<sub>2</sub>O<sub>3</sub> ( $x = 1-4$ ) catalytic systems. All the reduced catalysts exhibited similar diffraction patterns, indicating the presence of tetragonal ZrO<sub>2</sub> phase (at  $2\theta = 29.82, 49.76, 59.72$ ; JCPDS reference number 00-024-1164) and cubic Al<sub>2</sub>O<sub>3</sub> phase (at  $2\theta = 36.61, 39.07, 45.10, 59.72, 66.35$ ; JCPDS reference number 00-004-0858). Notably, the diffraction pattern of the reduced catalyst system appears to be much more intense compared with the fresh catalyst system (Figure S1). The fresh catalyst system has the cubic ZrO<sub>2</sub> phase (at  $2\theta = 30.29^\circ, 50.57^\circ, 60.48^\circ$ ; JCPDS reference number: 00-027-0997), whereas the reduced catalyst has the tetragonal ZrO<sub>2</sub> phase (Figure S1). In our study, the sample undergoes reduction at 600 °C. It has been reported that the energy difference between tetragonal ZrO<sub>2</sub> and cubic ZrO<sub>2</sub> increases with increasing temperature, and at high temperatures, the tetragonal phase becomes more stable than the cubic phase. Interestingly, in the fresh Sr-doped catalyst, the presence of the orthorhombic SrCO<sub>3</sub> phase (at  $2\theta = 25.1^\circ, 36.4^\circ, 45.5^\circ, 49.9^\circ$ ; JCPDS reference number: 00-001-0556) is observed.<sup>36,37</sup> However, in the reduced catalyst system, this phase is not detected, indicating that the reduction process leads to the disappearance or transformation of the

SrCO<sub>3</sub> phase. In both the fresh and reduced catalyst systems, Ni-related phases are not detected by XRD, indicating that Ni is finely dispersed beyond the detection limit of this technique. Sr (3d) XPS spectra at 134.2–135.9 eV binding energy, Al (2p) XPS spectra at 74.81 eV binding energy, and Zr (3d) XPS spectra at 182.9 eV binding energy confirms the +2 oxidation state of Sr, +3 oxidation state of Al, and +4 oxidation state of Zr, respectively (Figure 2B–D).<sup>38–40</sup> This information is valuable in understanding the chemical composition and surface properties of the catalyst, which play a crucial role in its catalytic activity during CO<sub>2</sub> methanation. All fresh and reduced catalysts show type IV adsorption–desorption isotherms with an H1 hysteresis loop, which confirms the presence of the model of mesopores (Figures 3 and S2).

The surface area, pore volume, and pore diameters of both Sr-promoted and unpromoted catalyst systems show similar values (Table 1). Before the methanation reaction, the catalyst is reduced, and thus, the surface parameters of the reduced catalyst system accurately represent the surface area and porosity of the catalyst before the reaction. Interestingly, the surface area and the pore volume of the reduced 5Ni/10ZrO<sub>2</sub>+Al<sub>2</sub>O<sub>3</sub> catalyst remain unchanged compared to the fresh catalyst, whereas in the Sr-promoted catalyst system (5Ni<sub>x</sub>Sr/10ZrO<sub>2</sub>+Al<sub>2</sub>O<sub>3</sub>;  $x = 1-4$  wt %), these parameters are decreased upon reduction of the catalyst (Figure S2). This observation suggests that Sr promotion may influence the surface properties of the catalyst upon reduction. The XRD analysis revealed that the diffraction pattern of the orthorhombic SrCO<sub>3</sub> phase disappears upon reduction. This indicates that the orthorhombic SrCO<sub>3</sub> phase undergoes restructuring and reduction during the reduction process. The  $d(V)/d(\log W)$  vs  $W$  plot shows a unimodal pore size

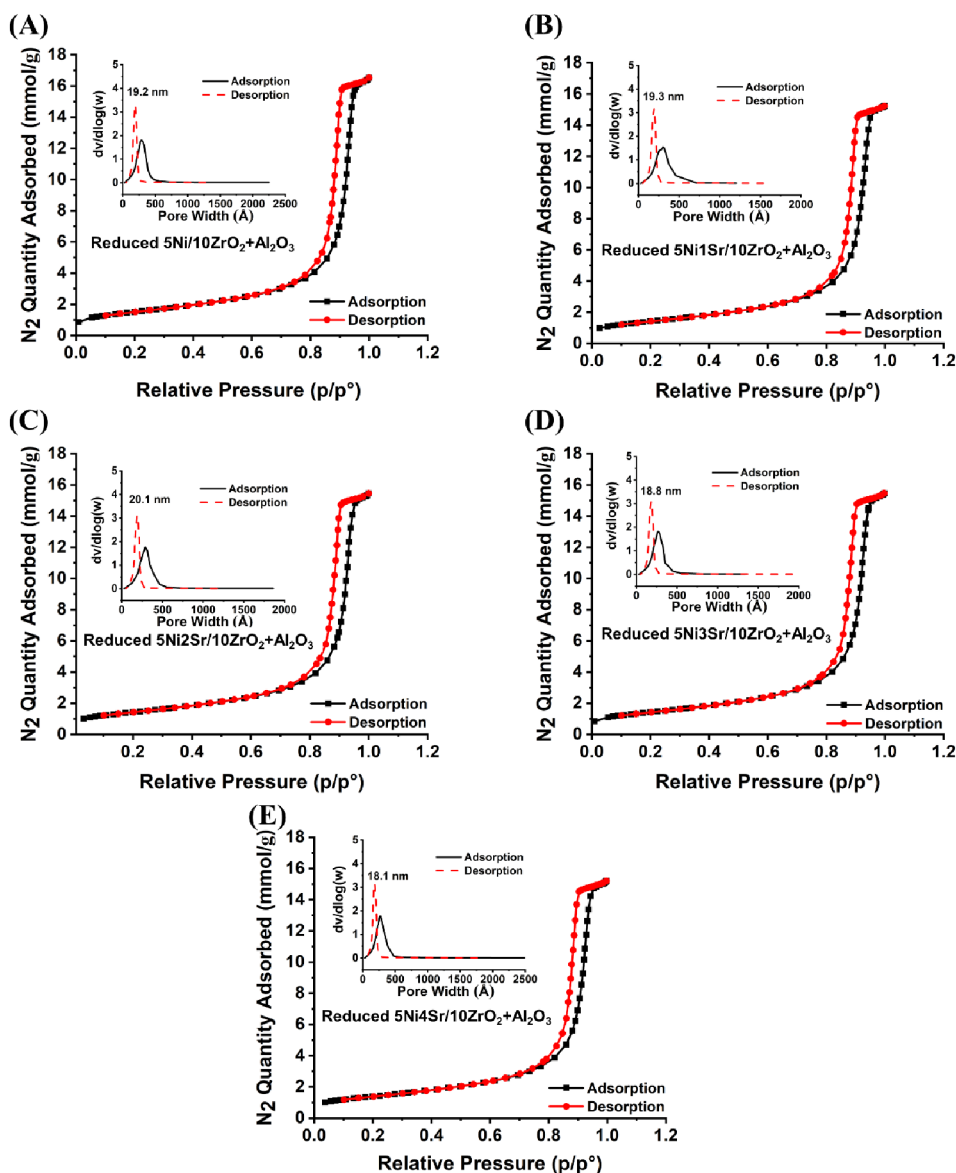


**Figure 3.** (A–E) Nitrogen sorption isotherm of reduced 5Ni<sub>x</sub>Sr/10ZrO<sub>2</sub>+Al<sub>2</sub>O<sub>3</sub> ( $x = 0–4$  wt %) catalyst system. The inset figure shows the porosity distribution of the reduced 5Ni<sub>x</sub>Sr/10ZrO<sub>2</sub>+Al<sub>2</sub>O<sub>3</sub> ( $x = 0–4$  wt %) catalyst system.

**Table 1.** Surface Area, Pore Volume, Pore Diameter, Ni Dispersion, CO<sub>2</sub> Conversion, and CH<sub>4</sub> Yield of 5Ni/10ZrO<sub>2</sub>+Al<sub>2</sub>O<sub>3</sub> and 5Ni<sub>x</sub>Sr/10ZrO<sub>2</sub>+Al<sub>2</sub>O<sub>3</sub> ( $x = 0–4$  wt %) Catalysts<sup>a</sup>

catalyst sample	surface area (m <sup>2</sup> /g)		pore volume (cm <sup>3</sup> /g)		pore size (nm)		Ni dispersion (mmol/g)	$X_{\text{CO}_2}$	$Y_{\text{CH}_4}$
	Fr.	Red.	Fr.	Red.	Fr.	Red.			
5Ni/10ZrO <sub>2</sub> +Al <sub>2</sub> O <sub>3</sub>	125	121.5	0.61	0.60	15.8	16.1	0.059	65	61
5Ni1Sr/10ZrO <sub>2</sub> +Al <sub>2</sub> O <sub>3</sub>	124.5	113.5	0.60	0.56	15.6	15.9	0.082	72.5	63.6
5Ni2Sr/10ZrO <sub>2</sub> +Al <sub>2</sub> O <sub>3</sub>	123.9	114.2	0.61	0.56	15.6	15.7	0.081	80.6	71.5
5Ni3Sr/10ZrO <sub>2</sub> +Al <sub>2</sub> O <sub>3</sub>	122.8	114.3	0.61	0.57	15.5	15.5	0.096	82.5	73.4
5Ni4Sr/10ZrO <sub>2</sub> +Al <sub>2</sub> O <sub>3</sub>	122.0	111.0	0.61	0.56	15.5	15.6	0.1	84.3	75.9

<sup>a</sup>Fr. = Fresh catalyst, Red. = Reduced catalyst,  $X_{\text{CO}_2}$  = CO<sub>2</sub> conversion,  $Y_{\text{CH}_4}$  = CH<sub>4</sub> yield.

distribution in all reduced catalyst systems, with the major pore volume being occupied by pores of 18–20 nm in all spent catalysts. This indicates that the reduction process affects the pore structure of the catalyst, leading to a similar unimodal pore size distribution dominated by pores of a specific size range in all the spent catalysts. These findings provide valuable insights into the structural changes occurring in the catalysts

during reduction and their implications for catalytic activity in the CO<sub>2</sub> methanation reaction.

The infrared spectra of the reduced catalyst systems showed relatively intense absorption bands corresponding to physically adsorbed CO<sub>2</sub> species at 2349 cm<sup>-1</sup>,<sup>41</sup> as well as format species at 2850 and 2925 cm<sup>-1</sup>,<sup>41</sup> which are more prominent compared to the fresh catalyst (Figure S3).

The temperature-programmed studies are carried out to understand the reducibility profile of fresh catalyst, the basicity profile of spent catalyst, and the acidity profile of the spent catalyst. The H<sub>2</sub>-TPR study confirms consumption of hydrogen in 400–630 °C and 630–1000 °C temperature range. The former signifies the amount of 'NiO-species which interacted with support with moderate interaction', while the latter is attributed to the amount of 'NiO-species which interacted strongly with the support' (Figure 4). Here, prior to the CO<sub>2</sub>

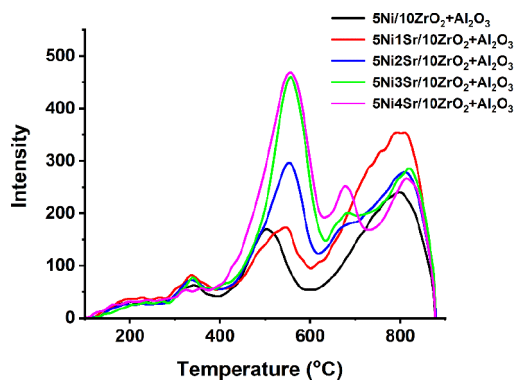


**Figure 4.** H<sub>2</sub>-temperature-programmed reduction study of 5Ni/10ZrO<sub>2</sub>+Al<sub>2</sub>O<sub>3</sub> and 5NixSr/10ZrO<sub>2</sub>+Al<sub>2</sub>O<sub>3</sub> (x = 1–4) catalysts.

methanation reaction, catalyst reduction was carried out at 700 °C under hydrogen. So up to 700 °C, mostly 'moderately interacting NiO-species' are reduced to metallic Ni. Furthermore, metallic Ni becomes the center for hydrogen dissociation during the CO<sub>2</sub> methanation reaction. Upon 1 wt

% addition of Sr over 5Ni/10ZrO<sub>2</sub>+Al<sub>2</sub>O<sub>3</sub>, the amount of 'moderately interacted NiO-species' is not affected. It is noticeable that upon increased loading of 1–4 wt % Sr over 5Ni/10ZrO<sub>2</sub>+Al<sub>2</sub>O<sub>3</sub>, the amount of 'moderately interacted NiO-species' is grown, and these NiO-species surges 'Ni' active sites upon reduction. The result of H<sub>2</sub>-chemisorption is in line with the H<sub>2</sub>-TPR results. The dispersion of metallic Ni over different catalysts is observed in the following order: 5Ni4Sr/10ZrO<sub>2</sub>+Al<sub>2</sub>O<sub>3</sub> (0.1 mmol/g) > 5Ni3Sr/10ZrO<sub>2</sub>+Al<sub>2</sub>O<sub>3</sub> (0.096 mmol/g) > 5Ni2Sr/10ZrO<sub>2</sub>+Al<sub>2</sub>O<sub>3</sub> (0.081 mmol/g) ~ 5Ni1Sr/10ZrO<sub>2</sub>+Al<sub>2</sub>O<sub>3</sub> (0.082 mmol/g) > 5Ni/10ZrO<sub>2</sub>+Al<sub>2</sub>O<sub>3</sub> (0.059 mmol/g).

Incorporating zirconia into alumina has been reported to increase the total acidity of the resulting zirconia–alumina composite compared to that of pure alumina. This increased acidity is valuable in catalysis, as it can facilitate various acid-catalyzed reactions and improve the overall catalytic performance of the material.<sup>42</sup> Cai et al. also reported the presence of weak basic sites over alumina–zirconia-supported Ni catalysts.<sup>19</sup> Over the current 10ZrO<sub>2</sub>+Al<sub>2</sub>O<sub>3</sub> support, the concentration of acid sites and basic sites is reported to be lower than that of ZrO<sub>2</sub> alone. Adding basic SrO or Sr(OH)<sub>2</sub> to an acidic zirconia–alumina-supported Ni catalyst can potentially weaken the acid profile on the catalyst surface. Previous studies have shown that SrCO<sub>3</sub> can enhance surface acidity over SrTiO<sub>3</sub>.<sup>43</sup> The formation of SrO enhances the basicity of the catalyst, while SrCO<sub>3</sub> may contribute to the acidity of the system. Overall, the acid–base profile of the catalyst plays a crucial role in directing the CO<sub>2</sub> methanation reaction. The balance between acidic and basic sites on the

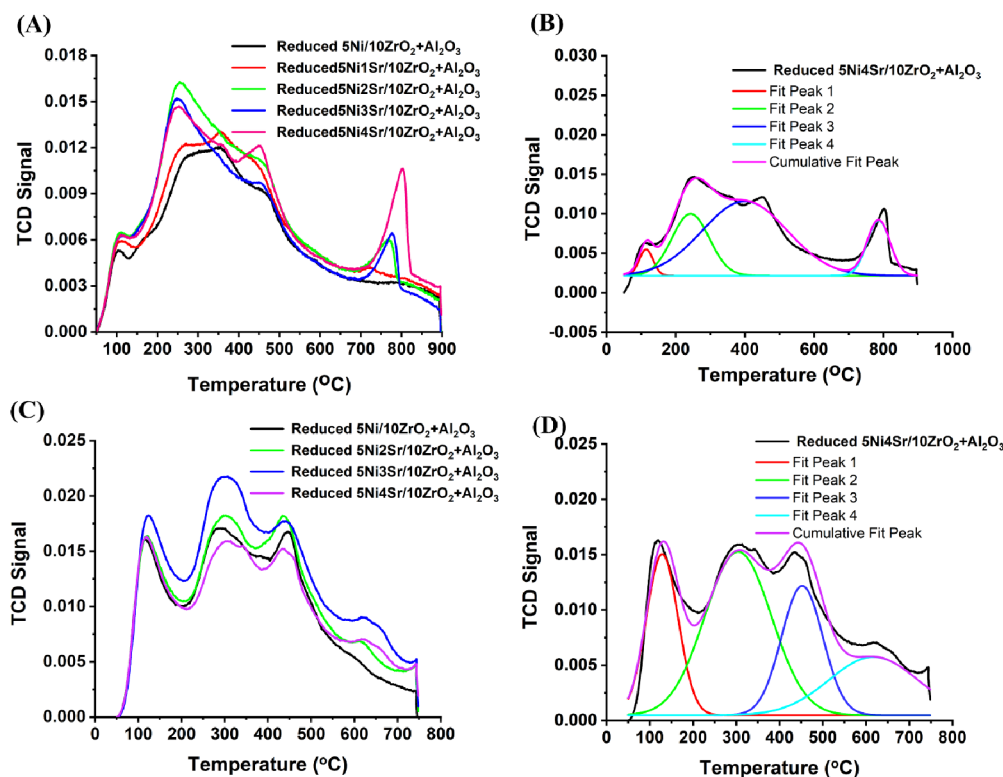


**Figure 5.** (A) CO<sub>2</sub>-temperature-programmed desorption profile of reduced 5NixSr/10ZrO<sub>2</sub>+Al<sub>2</sub>O<sub>3</sub> (x = 0–4 wt %) catalyst system, (B) peak fitting of CO<sub>2</sub>-TPD of the 5Ni4Sr/10ZrO<sub>2</sub>+Al<sub>2</sub>O<sub>3</sub> catalyst, (C) NH<sub>3</sub>-temperature-programmed desorption profile of reduced 5NixSr/10ZrO<sub>2</sub>+Al<sub>2</sub>O<sub>3</sub> (x = 0–4 wt %) catalyst system, (D) peak fitting of NH<sub>3</sub>-TPD of the 5Ni4Sr/10ZrO<sub>2</sub>+Al<sub>2</sub>O<sub>3</sub> catalyst.

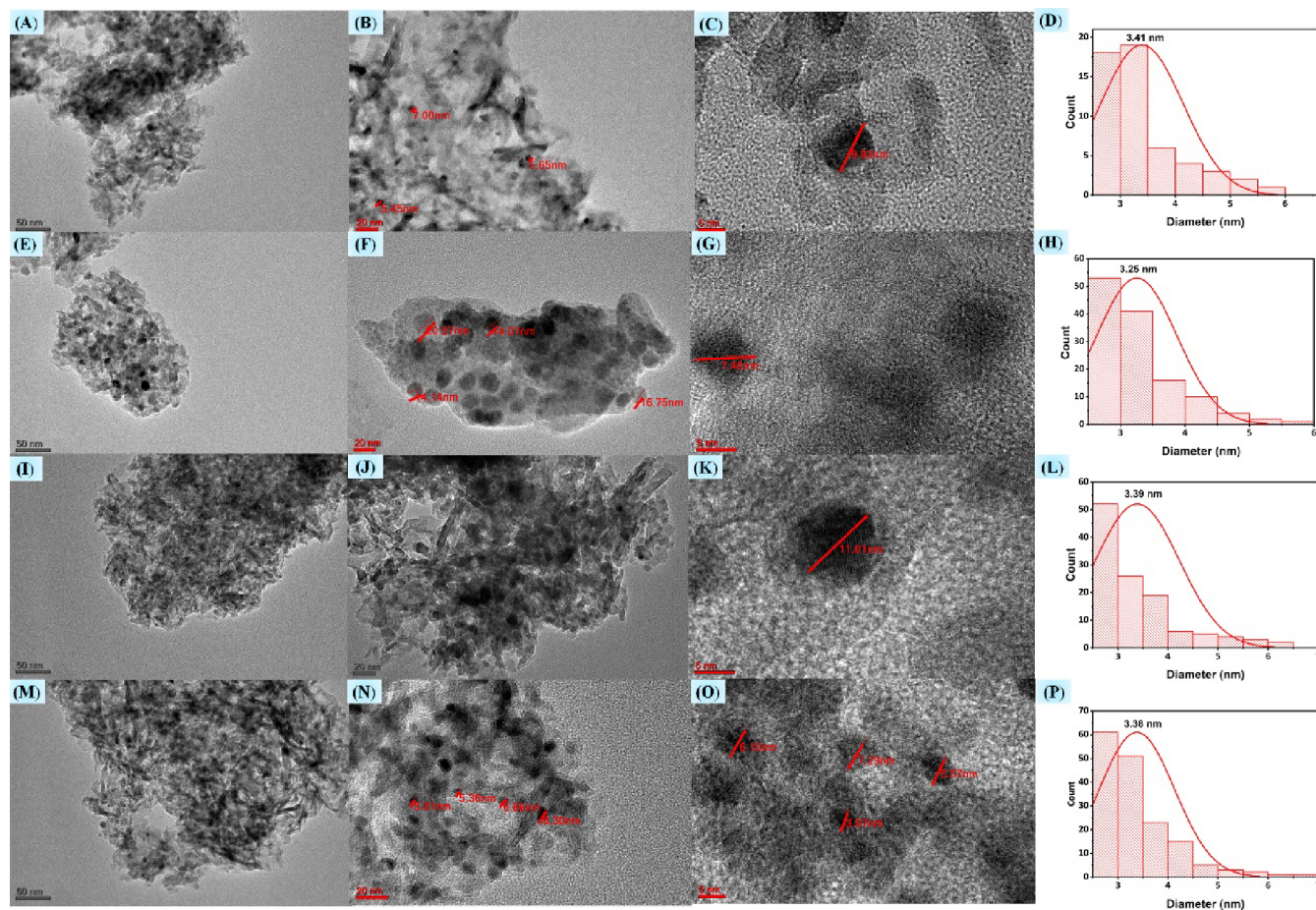


**Figure 6.** TEM images of (A–C) reduced 5Ni/10ZrO<sub>2</sub>+Al<sub>2</sub>O<sub>3</sub> at 50, 20, and 5 nm scale, (D) particle size distribution of reduced 5Ni/10ZrO<sub>2</sub>+Al<sub>2</sub>O<sub>3</sub>, (E–G) spent 5Ni/10ZrO<sub>2</sub>+Al<sub>2</sub>O<sub>3</sub> at 50, 20, and 5 nm scale, (H) particle size distribution of spent 5Ni/10ZrO<sub>2</sub>+Al<sub>2</sub>O<sub>3</sub>, (I–L) reduced 5Ni4Sr/10ZrO<sub>2</sub>+Al<sub>2</sub>O<sub>3</sub> at 50, 20, and 5 nm scale, (L) particle size distribution of reduced 5Ni4Sr/10ZrO<sub>2</sub>+Al<sub>2</sub>O<sub>3</sub>, (M–P) spent 5Ni4Sr/10ZrO<sub>2</sub>+Al<sub>2</sub>O<sub>3</sub> at 50, 20, and 5 nm scale, (P) particle size distribution of spent 5Ni4Sr/10ZrO<sub>2</sub>+Al<sub>2</sub>O<sub>3</sub>.

catalyst surface will determine its catalytic activity and selectivity for CO<sub>2</sub> methanation.

The basic profile of both fresh and reduced 5Ni<sub>x</sub>Sr/10ZrO<sub>2</sub>+Al<sub>2</sub>O<sub>3</sub> catalysts was investigated by CO<sub>2</sub> desorption (Figures 5A,B and S4). The fresh 5Ni/10ZrO<sub>2</sub>+Al<sub>2</sub>O<sub>3</sub> catalyst exhibited a diffused desorption peak around 100 °C, corresponding to a weak basic site (CO<sub>2</sub> adsorbed over surface hydroxyl-generating HCO<sub>3</sub><sup>−</sup> species) and a broad peak in the region of 250–450 °C, attributed to moderate strength basic sites (CO<sub>2</sub> adsorbed over surface oxide ion).<sup>44–46</sup> After reduction, the CO<sub>2</sub>-TPD profile of the reduced catalyst represents the actual basic sites present on the catalyst surface. The reducible surface hydroxyl (constituting weak basic sites) and reducible surface oxide ion (constituting moderate basic sites) are reduced during this process, leading to a decrease in the intensity of basic sites on the reduced catalyst compared to the fresh catalyst.

In the fresh Sr-doped 5Ni/10ZrO<sub>2</sub>+Al<sub>2</sub>O<sub>3</sub> catalyst, CO<sub>2</sub> desorption peaks are observed at 600 and 800 °C, indicating the presence of strontium-related/induced structures (Figure S4). The interaction between basic surface oxygen (including Sr–O) and CO<sub>2</sub> was found to generate ‘bonded carbonate species,’ which is decomposed at about 600 °C.<sup>46</sup> Zhao et al. also claimed that the CO<sub>2</sub> desorption peak, around 600 °C, is for decomposing highly dispersed SrCO<sub>3</sub> species.<sup>47</sup> Interestingly, this peak was not observed in the reduced catalyst,

indicating that it decomposes under H<sub>2</sub> steam during reduction at 700 °C. As a result, this basic site does not exist after the reductive treatment of the catalyst. The disappearance of the orthorhombic SrCO<sub>3</sub> phase in XRD upon reduction supports this finding.

Another CO<sub>2</sub> desorption peak at around 800 °C is observed in both fresh and reduced catalysts, and its intensity increases with increasing Sr loading. Ghorbaei et al. reported effective CO<sub>2</sub> diffusivity in the SrCO<sub>3</sub> layer at >800 °C.<sup>47</sup> Although no other crystalline peaks of Sr-related compounds were found in the XRD of the reduced 5Ni<sub>x</sub>Sr/10ZrO<sub>2</sub>+Al<sub>2</sub>O<sub>3</sub> (x = 1–4) catalyst, an organization of amorphous strong basic sites may be present over the Sr-promoted catalyst, constituted by –Sr–O– and –C–O– like species. This suggests that the addition of Sr promotes the formation of strong basic sites on the catalyst surface, which may play a crucial role in guiding the CO<sub>2</sub> methanation reaction.

To investigate the surface acidity profile, NH<sub>3</sub>-TPD of both fresh and reduced 5Ni<sub>x</sub>Sr/10ZrO<sub>2</sub>+Al<sub>2</sub>O<sub>3</sub> catalysts was conducted (Figures 5C,D and S5). The unpromoted catalyst exhibited a desorption peak of ammonia in a low-temperature region (~100 °C) for physisorbed NH<sub>3</sub> and a peak at ~300 °C for chemisorbed NH<sub>3</sub>, indicating the presence of weak acid sites (Figure 5SA).<sup>48</sup> In contrast, the Sr-promoted 5Ni/10ZrO<sub>2</sub>+Al<sub>2</sub>O<sub>3</sub> catalyst showed an additional peak in the high-temperature region (600–700 °C) for strong acid sites.<sup>49</sup> It

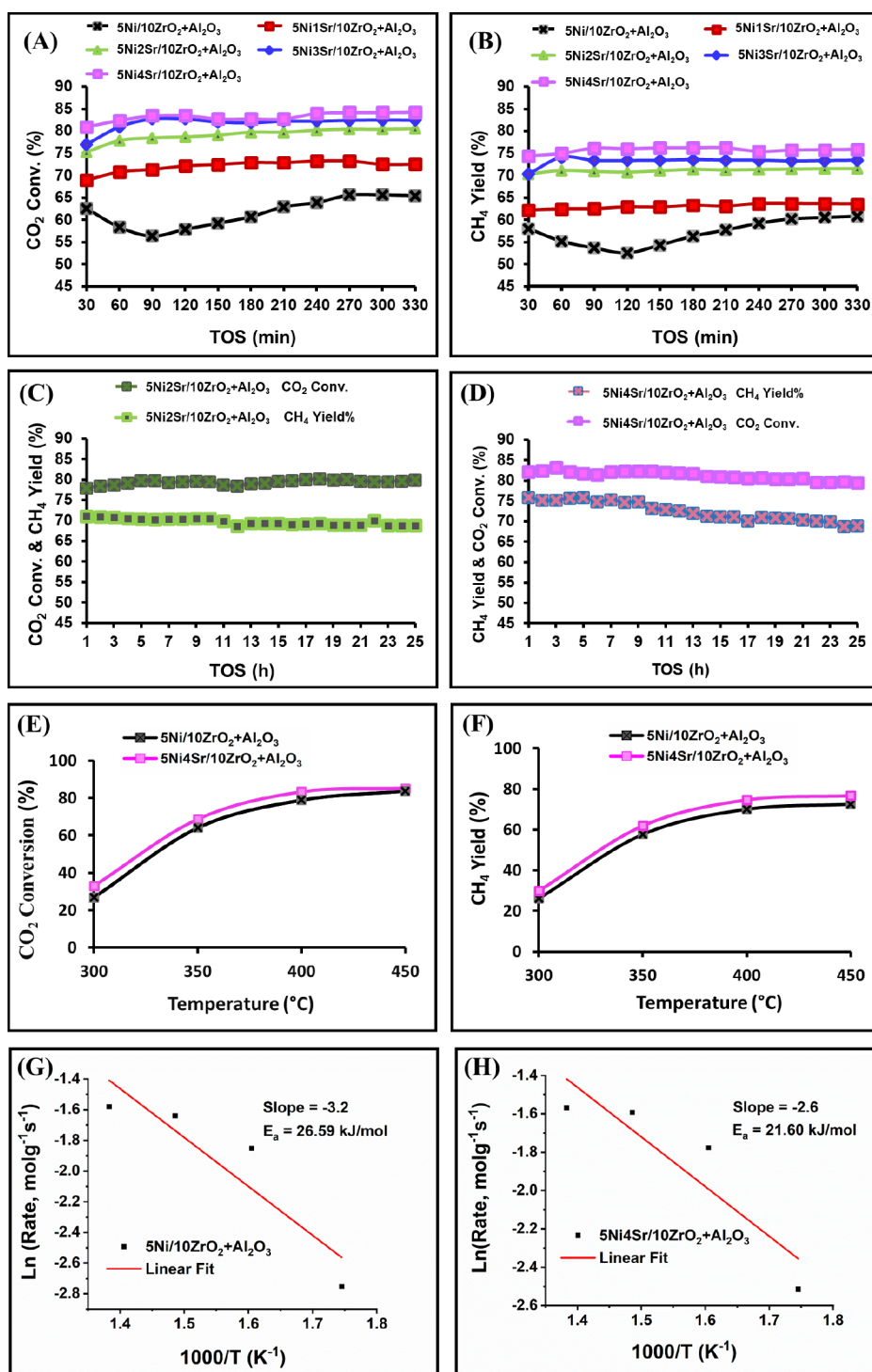


**Figure 7.** Catalytic activity results of CO<sub>2</sub>: H<sub>2</sub>: Ar (1:4:5 volume ratio) at 6000 ccg<sup>-1</sup>h<sup>-1</sup> GHSV: (A) CO<sub>2</sub> conversion % vs 330 min TOS over different catalysts at 400 °C; (B) CH<sub>4</sub> yield (%) vs 330 min TOS over different catalysts at 400 °C conversion; (C) 'CO<sub>2</sub> conversion (%) and CH<sub>4</sub> yield (%)' vs long TOS over the Ni<sub>2</sub>Sr/10ZrO<sub>2</sub>+Al<sub>2</sub>O<sub>3</sub> catalyst at 400 °C; (D) 'CO<sub>2</sub> conversion (%) and CH<sub>4</sub> yield (%)' vs long TOS over the Ni<sub>2</sub>Sr/10ZrO<sub>2</sub>+Al<sub>2</sub>O<sub>3</sub> catalyst at 400 °C; (E) CO<sub>2</sub> conversion (%) vs reaction temperature over reduced Ni/10ZrO<sub>2</sub>+Al<sub>2</sub>O<sub>3</sub> and reduced Ni<sub>4</sub>Sr/10ZrO<sub>2</sub>+Al<sub>2</sub>O<sub>3</sub> catalysts; (F) CH<sub>4</sub> yield (%) vs reaction temperature over reduced Ni/10ZrO<sub>2</sub>+Al<sub>2</sub>O<sub>3</sub> and reduced Ni<sub>4</sub>Sr/10ZrO<sub>2</sub>+Al<sub>2</sub>O<sub>3</sub> catalysts; (G) plot of ln(rate, molg<sup>-1</sup>h<sup>-1</sup>) vs 1000/T (K<sup>-1</sup>) for getting slope and apparent activation energy over 5Ni/10ZrO<sub>2</sub>+Al<sub>2</sub>O<sub>3</sub>; (H) plot of ln(rate, molg<sup>-1</sup>h<sup>-1</sup>) vs 1000/T (K<sup>-1</sup>) for getting slope and apparent activation energy over 5Ni<sub>4</sub>Sr/10ZrO<sub>2</sub>+Al<sub>2</sub>O<sub>3</sub>.

indicates that the reduction peak of about 600 °C is related to acidity borne by Sr species. Since the CO<sub>2</sub> methanation reaction was performed over a reduced catalyst, the acid profile over the reduced catalyst reflects the actual acid sites during the reaction. The weak acid sites are associated with the acidity

provided by the surface hydroxyl groups. After the catalyst reduction, the reducible surface hydroxyl groups are converted to water, leading to a decrease in the total surface hydroxyl concentration on the catalyst surface. As a result, when NH<sub>3</sub>-TPD is conducted with the reduced catalyst system, the peak

intensity at around  $\sim 300$  °C (for weak acidity) is decreased compared to the fresh catalyst system (Figures 5B and 5SB–G). Additionally, over the reduced Sr-promoted 5Ni/10ZrO<sub>2</sub>+Al<sub>2</sub>O<sub>3</sub> catalyst, the intensity of the strong acid site at around 650 °C is reduced, while a new desorption peak at about 450 °C for moderate-strength acid sites is observed (compared with the fresh catalyst). The new NH<sub>3</sub> desorption peak about 450 °C is also observed over reduced nonpromoted catalyst. It means that the acid sites reflecting around 450 °C in the NH<sub>3</sub>-TPD profile are not due to Sr species. It can be correlated to moderate strength acid sites, which are created after reduction of the catalyst.

TEM images of reduced and spent 5Ni/10ZrO<sub>2</sub>+Al<sub>2</sub>O<sub>3</sub> and 5Ni4Sr/10ZrO<sub>2</sub>+Al<sub>2</sub>O<sub>3</sub> catalysts are shown in Figure 6. The particle sizes of both catalytic systems remain consistent, ranging from 3.28 to 3.41 nm over reduced and spent catalysts.

**3.2. Catalytic Activity Results and Discussion.** The catalytic activities of reduced Ni/10ZrO<sub>2</sub>+Al<sub>2</sub>O<sub>3</sub> and reduced Ni<sub>x</sub>Sr/10ZrO<sub>2</sub>+Al<sub>2</sub>O<sub>3</sub> ( $x = 1-4$ ) catalysts are presented in Figure 7. During the reduction process, the active sites ‘Ni’ are derived mostly from ‘moderately interacted NiO-species’ over the catalyst. Along with the formation of active sites, various physio-chemical modifications are also observed during catalyst reduction. In the fresh catalyst system, cubic phases of ZrO<sub>2</sub> and Al<sub>2</sub>O<sub>3</sub> are present, while in the reduced catalyst system, intense tetragonal ZrO<sub>2</sub> and cubic Al<sub>2</sub>O<sub>3</sub> phases are observed. The tetragonal ZrO<sub>2</sub> phase is more stable at high temperatures compared to cubic ZrO<sub>2</sub>. Furthermore, the reduced catalyst exhibits a higher intensity of CO<sub>2</sub>-adsorbed species, such as formate species, even at atmospheric pressure and normal temperature (confirmed by IR), compared to that of the fresh catalyst sample. The reduced catalyst also possesses weak and moderate strength basic sites, which are constituted by nonreducible surface hydroxyl and nonreducible surface oxide ions. The total amount of acid sites is decreased upon reduction of the 5Ni/10ZrO<sub>2</sub>+Al<sub>2</sub>O<sub>3</sub> catalyst (confirmed by NH<sub>3</sub>-TPD).

The catalytic activity of reduced Ni/10ZrO<sub>2</sub>+Al<sub>2</sub>O<sub>3</sub> catalysts showed fluctuations initially but stabilized after 270 min. This catalyst exhibited 65% CO<sub>2</sub> conversion with 61% CH<sub>4</sub> yield during the 330 min time on stream at 400 °C reaction temperature. Previous literature has reported a slow decline in CO<sub>2</sub> conversion for the 20Ni/Al<sub>2</sub>O<sub>3</sub> catalyst.<sup>18</sup> Salamony et al. found a rapid drop in CO<sub>2</sub> conversion from 16% to 0% within 30 min over a zirconia-supported Ni catalyst.<sup>13</sup> Cai et al. observed the stabilization of catalytic active sites Ni upon incorporation of ZrO<sub>2</sub> along with the Al<sub>2</sub>O<sub>3</sub>.<sup>19</sup> They found constant catalytic activity ( $\sim 40\%$  CO<sub>2</sub> conversion) over a Ni-impregnated alumina–zirconia catalyst. In our case, constant catalytic activity was achieved after a 270 min over reduced Ni/10ZrO<sub>2</sub>+Al<sub>2</sub>O<sub>3</sub> catalysts. Notably, over a reduced Ni/10ZrO<sub>2</sub>+Al<sub>2</sub>O<sub>3</sub> catalyst, CO was not detected, indicating that the methanation reaction of CO<sub>2</sub> occurred through a direct pathway (without involving CO in the reaction steps as an intermediate).

The reduced 5Ni<sub>x</sub>Sr/10ZrO<sub>2</sub>+Al<sub>2</sub>O<sub>3</sub> ( $x = 1-4$ ) catalysts demonstrated good dispersion of Ni after reduction. After reduction, a noticeable drop in the surface area and pore volume was observed, which is expected for surface modification after the reduction process. A disappearance of SrCO<sub>3</sub> phases (confirmed by XRD and CO<sub>2</sub>-TPD) and a decrease in concentration of total acidity (confirmed by NH<sub>3</sub>-TPD) were noticed upon reduction of Sr-promoted 5Ni/

10ZrO<sub>2</sub>+Al<sub>2</sub>O<sub>3</sub> catalysts. Upon increasing the Sr loading from 1 to 4 wt % over 5Ni/10ZrO<sub>2</sub>+Al<sub>2</sub>O<sub>3</sub>, a higher density of ‘moderately interacted NiO species’ are cultivated, which facilitates a higher density of active sites ‘Ni’ after reduction. Again, by increasing the addition of Sr up to 4 wt %, the reduced catalyst system exhibited a higher concentration of strong basic sites and a noticeable concentration of moderate-strength acid sites. Upon Sr promotional addition over reduced-Ni/10ZrO<sub>2</sub>+Al<sub>2</sub>O<sub>3</sub>, the constant activity was obtained within 60 min. The CO<sub>2</sub> conversion ( $X_{\text{CO}_2}$ ) and CH<sub>4</sub> yield ( $Y_{\text{CH}_4}$ ) increased with increasing Sr loading over the 5Ni/10ZrO<sub>2</sub>+Al<sub>2</sub>O<sub>3</sub> catalyst, with the following trend: 5Ni4Sr/10ZrO<sub>2</sub>+Al<sub>2</sub>O<sub>3</sub> ( $X_{\text{CO}_2} = 84.3\%$ ,  $Y_{\text{CH}_4} = 75.9\%$ ) > 5Ni3Sr/10ZrO<sub>2</sub>+Al<sub>2</sub>O<sub>3</sub> ( $X_{\text{CO}_2} = 82.5\%$ ,  $Y_{\text{CH}_4} = 73.4\%$ ) > 5Ni2Sr/10ZrO<sub>2</sub>+Al<sub>2</sub>O<sub>3</sub> ( $X_{\text{CO}_2} = 80.6\%$ ,  $Y_{\text{CH}_4} = 71.5\%$ ) > 5Ni1Sr/10ZrO<sub>2</sub>+Al<sub>2</sub>O<sub>3</sub> ( $X_{\text{CO}_2} = 72.5\%$ ,  $Y_{\text{CH}_4} = 63.6\%$ ) > 5Ni/10ZrO<sub>2</sub>+Al<sub>2</sub>O<sub>3</sub> ( $X_{\text{CO}_2} = 65\%$ ,  $Y_{\text{CH}_4} = 61\%$ ). Before dwelling in deep discussion, the major characterization and activity results are summarized in Table 1.

Interestingly, the dispersion of Ni sites over 5Ni1Sr/10ZrO<sub>2</sub>+Al<sub>2</sub>O<sub>3</sub> and 5Ni3Sr/10ZrO<sub>2</sub>+Al<sub>2</sub>O<sub>3</sub> catalysts are 1.38 and 1.62 times than the unpromoted catalyst (5Ni/10ZrO<sub>2</sub>+Al<sub>2</sub>O<sub>3</sub>) (Table 1). As per the rise in Ni dispersion, the CO<sub>2</sub> conversion has also increased up to 72.5% and 82.5% over 5Ni1Sr/10ZrO<sub>2</sub>+Al<sub>2</sub>O<sub>3</sub> and 5Ni3Sr/10ZrO<sub>2</sub>+Al<sub>2</sub>O<sub>3</sub>, respectively. Upon increasing Sr loading from 1 to 2 wt % and 3 to 4 wt % over 5Ni/10ZrO<sub>2</sub>+Al<sub>2</sub>O<sub>3</sub>, the dispersion of active sites ‘Ni’ does not vary much, but CO<sub>2</sub> conversion always grows markedly. CO<sub>2</sub>-TPD profile shows that the concentration of strong basic sites is increasing when strontium loading is increased from 1 to 2 wt % and from 3 to 4 wt %. Ni sites initiate hydrogen dissociation, whereas basic sites stabilize the CO<sub>2</sub>-interacted species over the surface. CO<sub>2</sub>-interacted species interact with dissociated hydrogen and undergo a methanation reaction. Now, it is clear that the catalytic activity depends on the dispersion of Ni sites as well as the extent of stabilization of the CO<sub>2</sub>-interacted species.

The long-term stability of the 5Ni2Sr/10ZrO<sub>2</sub>+Al<sub>2</sub>O<sub>3</sub> and 5Ni4Sr/10ZrO<sub>2</sub>+Al<sub>2</sub>O<sub>3</sub> catalysts at 400 °C was also studied (Figure 7C,D). The catalytic performance of the 5Ni2Sr/10ZrO<sub>2</sub>+Al<sub>2</sub>O<sub>3</sub> catalyst is found to be slightly more consistent than that of the 5Ni4Sr/10ZrO<sub>2</sub>+Al<sub>2</sub>O<sub>3</sub> catalyst. To explain the high CO<sub>2</sub> conversion ( $\sim 80\%$ ) and CH<sub>4</sub> yield ( $\sim 70\%$ ) observed for up to 28 h in time on stream test through the direct pathway over the 5Ni4Sr/10ZrO<sub>2</sub>+Al<sub>2</sub>O<sub>3</sub> catalyst, several factors need to be considered. First, the strontium-promoted zirconia–alumina-supported Ni catalyst appears to have the highest density of active sites ‘Ni’ with optimum dispersion. Second, the unique acido-basic profile of the 5Ni4Sr/10ZrO<sub>2</sub>+Al<sub>2</sub>O<sub>3</sub> catalyst, characterized by the highest concentration of strong basic sites and noticeable concentration of moderate strength acid sites, likely contributes to the enhanced catalytic performance. These specific acid–base sites facilitate the adsorption and activation of CO<sub>2</sub> and H<sub>2</sub>, whereas the highest density of active sites endorses H<sub>2</sub> dissociation in time for sequential hydrogenation of formate species into hydroxy methyl  $\rightarrow$  methyl  $\rightarrow$  methane.

The mass transfer limitation over catalyst samples is calculated according to the Mears criterion and Weisz–Prater criterion.<sup>50</sup> The details of the calculation for external mass transfer limitation and internal mass transfer limitation are

shown in Supporting Information S6 and Table S1. Mears criterion for external diffusion is found to be less than 0.15, whereas the Weisz–Prater criterion for internal diffusion is below 1 over each catalyst system. These values confirm the absence of external as well as internal mass transfer limitations over each catalyst system used in this study. The effect of temperature over activity and apparent activation energy for CO<sub>2</sub> conversion over 5Ni/10ZrO<sub>2</sub>+Al<sub>2</sub>O<sub>3</sub> and 4 wt % Sr-promoted 5Ni/10ZrO<sub>2</sub>+Al<sub>2</sub>O<sub>3</sub> catalysts are also studied (Figure 7E,F). CO<sub>2</sub> conversion and CH<sub>4</sub> yield increased sharply between 300 and 400 °C and slightly between 400 and 450 °C. The apparent activation energy for CO<sub>2</sub> conversion over 4 wt % Sr-promoted 5Ni/10ZrO<sub>2</sub>+Al<sub>2</sub>O<sub>3</sub> catalysts is found to be lower ( $E_a = 21.60$  kJ/mol) than the nonpromoted 5Ni/10ZrO<sub>2</sub>+Al<sub>2</sub>O<sub>3</sub> catalyst ( $E_a = 26.59$  kJ/mol) (Figure 7G,H). Additionally, the stabilization of Ni by incorporating zirconia into the catalyst structure plays a vital role in maintaining the active sites' integrity and stability during the reaction. Lastly, the large size of Sr<sup>2+</sup> in the catalyst provides a stabilization capacity for CO<sub>2</sub>-intermediate-like carbonate species. This stabilization effect is crucial for sustaining the reaction and promoting the sequential hydrogenation process that leads to the production of methane. Overall, the exceptional catalytic performance of the 5Ni4Sr/10ZrO<sub>2</sub>+Al<sub>2</sub>O<sub>3</sub> catalyst in terms of CO<sub>2</sub> conversion and CH<sub>4</sub> yield can be attributed to its unique acido-basic profile, presence of highest dense active sites 'Ni,' stabilization of Ni through the incorporation of zirconia, and the stabilization capacity of CO<sub>2</sub>-intermediate-like formate species due to the presence of large-sized Sr<sup>2+</sup> ions. These factors collectively enable the catalyst to efficiently guide the CO<sub>2</sub> methanation reaction through the direct pathway, leading to high methane production yields.

#### 4. CONCLUSION

The catalytic activity toward CO<sub>2</sub> methanation was found to depend on the dispersion of active Ni sites (derived from moderately interacted NO species) as well as the extent of stabilization of CO<sub>2</sub>-surface intermediate species. Upon 1 wt % loading of Sr over 5Ni/10ZrO<sub>2</sub>+Al<sub>2</sub>O<sub>3</sub>, the Ni dispersion over the catalyst surface grows in comparison to the unpromoted catalyst, whereas upon 2 wt % Sr loading, dispersion of Ni is not affected much, but the concentration of strong basic sites is increased markedly. Again, at 3 wt % Sr loading over 5Ni/10ZrO<sub>2</sub>+Al<sub>2</sub>O<sub>3</sub>, dispersion of Ni sites increases (in comparison to 5Ni2Sr/10ZrO<sub>2</sub>+Al<sub>2</sub>O<sub>3</sub>), while at 4 wt % Sr loading, concentration of strong basic sites increases significantly. The Sr-promoted 5Ni/10ZrO<sub>2</sub>+Al<sub>2</sub>O<sub>3</sub> catalyst has a lower apparent activation energy for CO<sub>2</sub> conversion than the unpromoted catalyst. The unique acido-basic profiles, characterized by strong basic and moderate acid sites, facilitate the sequential hydrogenation of format species into hydroxy methyl → methyl → methane. The 5Ni4Sr/10ZrO<sub>2</sub>+Al<sub>2</sub>O<sub>3</sub> catalyst demonstrates exceptional performance, achieving approximately 80% CO<sub>2</sub> conversion and 70% CH<sub>4</sub> yield for up to 25 h time on stream via the direct methanation pathway. In summary, the combination of zirconia–alumina support, Ni catalyst, and Sr promotion proves to be a highly efficient and stable system for CO<sub>2</sub> methanation, opening up new possibilities for CO<sub>x</sub>-free CH<sub>4</sub> production with potential applications in addressing environmental concerns and energy sustainability.

#### ■ ASSOCIATED CONTENT

##### Supporting Information

The Supporting Information is available free of charge at <https://pubs.acs.org/doi/10.1021/acsomega.3c08536>.

Figure S1: XRD pattern of 5Ni2Sr/10ZrO<sub>2</sub>+Al<sub>2</sub>O<sub>3</sub>. Figure S2: Nitrogen sorption isotherm of fresh and reduced 5Ni<sub>x</sub>Sr/10ZrO<sub>2</sub>+Al<sub>2</sub>O<sub>3</sub> ( $x = 0-4$  wt %) catalyst system. Figure S3: Infrared spectra of fresh and reduced 5Ni<sub>x</sub>Sr/10ZrO<sub>2</sub>+Al<sub>2</sub>O<sub>3</sub> ( $x = 0-4$  wt %) catalyst system. Figure S4: CO<sub>2</sub>-TPD profile over (A) fresh 5Ni/10ZrO<sub>2</sub>+Al<sub>2</sub>O<sub>3</sub>, (B) reduced 5Ni/10ZrO<sub>2</sub>+Al<sub>2</sub>O<sub>3</sub>O<sub>2</sub>, (C) fresh 5Ni1Sr/10ZrO<sub>2</sub>+Al<sub>2</sub>O<sub>3</sub> catalyst and reduced 5Ni1Sr/10ZrO<sub>2</sub>+Al<sub>2</sub>O<sub>3</sub> catalyst, (D) fresh 5Ni2Sr/10ZrO<sub>2</sub>+Al<sub>2</sub>O<sub>3</sub> catalyst and reduced 5Ni2Sr/10ZrO<sub>2</sub>+Al<sub>2</sub>O<sub>3</sub> catalyst, (E) fresh 5Ni3Sr/10ZrO<sub>2</sub>+Al<sub>2</sub>O<sub>3</sub> catalyst and reduced 5Ni3Sr/10ZrO<sub>2</sub>+Al<sub>2</sub>O<sub>3</sub> catalyst, (F) fresh 5Ni4Sr/10ZrO<sub>2</sub>+Al<sub>2</sub>O<sub>3</sub> catalyst and reduced 5Ni4Sr/10ZrO<sub>2</sub>+Al<sub>2</sub>O<sub>3</sub> catalyst. Figure S5; NH<sub>3</sub>-TPD profile over (A) fresh 5Ni<sub>x</sub>Sr/10ZrO<sub>2</sub>+Al<sub>2</sub>O<sub>3</sub> ( $x = 0-4$  wt %) catalyst, (B) fresh 5Ni/10ZrO<sub>2</sub>+Al<sub>2</sub>O<sub>3</sub> and reduced 5Ni/10ZrO<sub>2</sub>+Al<sub>2</sub>O<sub>3</sub>O<sub>2</sub>, (C) fresh 5Ni1Sr/10ZrO<sub>2</sub>+Al<sub>2</sub>O<sub>3</sub> catalyst and reduced 5Ni1Sr/10ZrO<sub>2</sub>+Al<sub>2</sub>O<sub>3</sub> catalyst, (D) fresh 5Ni2Sr/10ZrO<sub>2</sub>+Al<sub>2</sub>O<sub>3</sub> catalyst and reduced 5Ni2Sr/10ZrO<sub>2</sub>+Al<sub>2</sub>O<sub>3</sub> catalyst, (E) fresh 5Ni3Sr/10ZrO<sub>2</sub>+Al<sub>2</sub>O<sub>3</sub> catalyst and reduced 5Ni3Sr/10ZrO<sub>2</sub>+Al<sub>2</sub>O<sub>3</sub> catalyst, (F) fresh 5Ni4Sr/10ZrO<sub>2</sub>+Al<sub>2</sub>O<sub>3</sub> catalyst and reduced 5Ni4Sr/10ZrO<sub>2</sub>+Al<sub>2</sub>O<sub>3</sub> catalyst. Figure S6: Calculation of Mass transfer limitation. Table S7: Rate of CO<sub>2</sub> conversion and Mears criterion for external diffusion limitation and Weisz criterion for internal diffusion limitation (PDF)

#### ■ AUTHOR INFORMATION

##### Corresponding Authors

**Ahmed S. Al-Fatesh** – Chemical Engineering Department, College of Engineering, King Saud University, Riyadh 11421, Saudi Arabia; Email: [aalfatesh@ksu.edu.sa](mailto:aalfatesh@ksu.edu.sa)

**Ahmed I. Osman** – School of Chemistry and Chemical Engineering, Queen's University Belfast, Belfast, Northern Ireland BT9 5AG, U.K.;  [orcid.org/0000-0003-2788-7839](https://orcid.org/0000-0003-2788-7839); Email: [aosmanahmed01@qub.ac.uk](mailto:aosmanahmed01@qub.ac.uk)

**Rawesh Kumar** – Department of Chemistry, Indus University, Ahmedabad, Gujarat 382115, India; Email: [kr.rawesh@gmail.com](mailto:kr.rawesh@gmail.com)

##### Authors

**Abdulaziz A. M. Abahussain** – Chemical Engineering Department, College of Engineering, King Saud University, Riyadh 11421, Saudi Arabia

**Yuvrajsinh B. Rajput** – Department of Chemistry, Indus University, Ahmedabad, Gujarat 382115, India

**Salwa B. Alreshaidan** – Chemical Engineering Department, College of Engineering, King Saud University, Riyadh 11421, Saudi Arabia

**Hamid Ahmed** – Chemical Engineering Department, College of Engineering, King Saud University, Riyadh 11421, Saudi Arabia

**Anis H. Fakeeha** – Chemical Engineering Department, College of Engineering, King Saud University, Riyadh 11421, Saudi Arabia

Abdulrhman S. Al-Awadi – *Chemical Engineering Department, College of Engineering, King Saud University, Riyadh 11421, Saudi Arabia*

Radwa A. El-Salamony – *Process Development Department, Egyptian Petroleum Research Institute (EPRI), Cairo 11727, Egypt*

Complete contact information is available at:

<https://pubs.acs.org/10.1021/acsomega.3c08536>

## Notes

The authors declare no competing financial interest.

## ACKNOWLEDGMENTS

The authors would like to extend their sincere appreciation to Researchers Supporting Project number (RSP2024R368), King Saud University.

## REFERENCES

- (1) Anwar, M. N.; Fayyaz, A.; Sohail, N. F.; Khokhar, M. F.; Baqar, M.; Yasar, A.; Rasool, K.; Nazir, A.; Raja, M. U. F.; Rehan, M.; Aghbashlo, M.; Tabatabaei, M.; Nizami, A. S. CO<sub>2</sub> Utilization: Turning Greenhouse Gas into Fuels and Valuable Products. *J. Environ. Manage.* **2020**, *260*, 110059.
- (2) Mebrahtu, C.; Krebs, F.; Abate, S.; Perathoner, S.; Centi, G.; Palkovits, R. *CO<sub>2</sub> Methanation: Principles and Challenges*, 1st ed.; Elsevier, 2019; Vol. 178.
- (3) Frontera, P.; Macario, A.; Ferraro, M.; Antonucci, P. L. Supported Catalysts for CO<sub>2</sub> Methanation: A Review. *Catalysts* **2017**, *7* (2), 59.
- (4) Sheehan, S. W. Electrochemical Methane Production from CO<sub>2</sub> for Orbital and Interplanetary Refueling. *iScience* **2021**, *24* (3), 102230.
- (5) Ren, J.; Lou, H.; Xu, N.; Zeng, F.; Pei, G.; Wang, Z. Methanation of CO/CO<sub>2</sub> for Power to Methane Process: Fundamentals, Status, and Perspectives. *J. Energy Chem.* **2023**, *80*, 182–206.
- (6) Gómez, L.; Martínez, I.; Navarro, M. V.; Murillo, R. Selection and Optimisation of a Zeolite/Catalyst Mixture for Sorption-Enhanced CO<sub>2</sub> Methanation (SEM) Process. *J. CO<sub>2</sub> Util.* **2023**, *77*, 102611.
- (7) Tan, C. H.; Nomanbhay, S.; Shamsuddin, A. H.; Park, Y. K.; Hernández-Cocoletzi, H.; Show, P. L. Current Developments in Catalytic Methanation of Carbon Dioxide—A Review. *Front. Energy Res.* **2022**, *9*, 795423.
- (8) Dreyer, J. A. H.; Li, P.; Zhang, L.; Beh, G. K.; Zhang, R.; Sit, P. H. L.; Teoh, W. Y. Influence of the Oxide Support Reducibility on the CO<sub>2</sub> Methanation over Ru-Based Catalysts. *Appl. Catal., B* **2017**, *219*, 715–726.
- (9) Shen, L.; Xu, J.; Zhu, M.; Han, Y. F. Essential Role of the Support for Nickel-Based CO<sub>2</sub> Methanation Catalysts. *ACS Catal.* **2020**, *10* (24), 14581–14591.
- (10) Fakeeha, A. H.; Al-Fatesh, A. S.; Srivastava, V. K.; Ibrahim, A. A.; Abahussain, A. A. M.; Abu-Dahrieh, J. K.; Alotibi, M. F.; Kumar, R. Hydrogen Production from Gadolinium-Promoted Yttrium-Zirconium-Supported Ni Catalysts through Dry Methane Reforming. *ACS Omega* **2023**, *8* (24), 22108–22120.
- (11) Baiker, A.; Kilo, M.; Maciejewski, M.; Menzi, S.; Wokaun, A. Hydrogenation of CO<sub>2</sub> Over Copper, Silver and Gold/Zirconia Catalysts: Comparative Study of Catalyst Properties and Reaction Pathways. *Stud. Surf. Sci. Catal.* **1993**, *75*, 1257–1272.
- (12) Yamasaki, M.; Komori, M.; Akiyama, E.; Habazaki, H.; Kawashima, A.; Asami, K.; Hashimoto, K. CO<sub>2</sub> Methanation Catalysts Prepared from Amorphous Ni-Zr-Sm and Ni-Zr-Misch Metal Alloy Precursors. *Mater. Sci. Eng., A* **1999**, *267* (2), 220–226.
- (13) El-Salamony, R. A.; Acharya, K.; Al-Fatesh, A. S.; Osman, A. I.; Alreshaidan, S. B.; Kumar, N. S.; Ahmed, H.; Kumar, R. Enhanced Direct Methanation of CO<sub>2</sub> Using Ni-Based Catalysts Supported on ZrO<sub>2</sub>, CeO<sub>2</sub>-ZrO<sub>2</sub>, and La<sub>2</sub>O<sub>3</sub>-ZrO<sub>2</sub>: The Effect of Support Material on the Reducible NiO-Interacted Species and Catalytic Activity. *Mol. Catal.* **2023**, *547*, 113378.
- (14) Fu, H.; Sun, S.; Lian, H. Enhanced Low-Temperature CO<sub>2</sub> methanation over Ni/ ZrO<sub>2</sub>-Al<sub>2</sub>O<sub>3</sub> catalyst: Effect of Al Addition on Catalytic Performance and Reaction Mechanism. *J. CO<sub>2</sub> Util.* **2023**, *69*, 102415.
- (15) Acharya, K.; Al-Fatesh, A. S.; Almutairi, G.; Fakeeha, A. H.; Ibrahim, A. A.; Abasaeed, A. E.; Siddiqui, M. R. H.; Kumar, R. The Role of Strontium as an Economic Promoter Over WO<sub>3</sub> + ZrO<sub>2</sub> Supported Ni Catalyst for H<sub>2</sub> Production Through Dry Reforming of Methane. *Catal. Lett.* **2023**, 1–13.
- (16) Riani, P.; Spennati, E.; Garcia, M. V.; Escibano, V. S.; Busca, G.; Garbarino, G. Ni/Al<sub>2</sub>O<sub>3</sub> Catalysts for CO<sub>2</sub> Methanation: Effect of Silica and Nickel Loading. *Int. J. Hydrogen Energy* **2023**, *48* (64), 24976–24995.
- (17) Alrafei, B.; Polaert, I.; Ledoux, A.; Azzolina-Jury, F. Remarkably Stable and Efficient Ni and Ni-Co Catalysts for CO<sub>2</sub> Methanation. *Catalysis Today* **2020**, *346*, 23–33.
- (18) Rahmani, S.; Rezaei, M.; Meshkani, F. Preparation of Highly Active Nickel Catalysts Supported on Mesoporous Nanocrystalline  $\gamma$ -Al<sub>2</sub>O<sub>3</sub> for CO<sub>2</sub> Methanation. *J. Ind. Eng. Chem.* **2014**, *20* (4), 1346–1352.
- (19) Cai, M.; Wen, J.; Chu, W.; Cheng, X.; Li, Z. Methanation of Carbon Dioxide on Ni/ZrO<sub>2</sub>-Al<sub>2</sub>O<sub>3</sub> Catalysts: Effects of ZrO<sub>2</sub> Promoter and Preparation Method of Novel ZrO<sub>2</sub>-Al<sub>2</sub>O<sub>3</sub> Carrier. *J. Nat. Gas Chem.* **2011**, *20* (3), 318–324.
- (20) He, F.; Zhuang, J.; Lu, B.; Liu, X.; Zhang, J.; Gu, F.; Zhu, M.; Xu, J.; Zhong, Z.; Xu, G.; Su, F. Ni-Based Catalysts Derived from Ni-Zr-Al Ternary Hydrotalcites Show Outstanding Catalytic Properties for Low-Temperature CO<sub>2</sub> Methanation. *Appl. Catal., B* **2021**, *293*, 120218.
- (21) Wang, H.; Li, Z.; Cui, G.; Wei, M. Synergistic Catalysis at the Ni/ZrO<sub>2</sub>-x Interface toward Low-Temperature CO<sub>2</sub> Methanation. *ACS Appl. Mater. Interfaces* **2023**, *15* (15), 19021–19031.
- (22) Riani, P.; Valsamakis, I.; Cavattoni, T.; Sanchez Escibano, V.; Busca, G.; Garbarino, G. Ni/SiO<sub>2</sub>-Al<sub>2</sub>O<sub>3</sub> Catalysts for CO<sub>2</sub> Methanation: Effect of La<sub>2</sub>O<sub>3</sub> Addition. *Appl. Catal., B* **2021**, *284*, 119697.
- (23) Moghaddam, S. V.; Rezaei, M.; Meshkani, F.; Daroughegi, R. Synthesis of Nanocrystalline Mesoporous Ni/Al<sub>2</sub>O<sub>3</sub>-SiO<sub>2</sub> Catalysts for CO<sub>2</sub> Methanation Reaction. *Int. J. Hydrogen Energy* **2018**, *43* (41), 19038–19046.
- (24) Tamimi, K.; Alavi, S. M.; Rezaei, M.; Akbari, E. Preparation of the Mn-Promoted NiO-Al<sub>2</sub>O<sub>3</sub> Nanocatalysts for Low Temperature CO<sub>2</sub> Methanation. *J. Energy Inst.* **2021**, *99*, 48–58.
- (25) Rajabzadeh Nobakht, A.; Rezaei, M.; Alavi, S. M.; Akbari, E.; Varbar, M.; Hafezi-Bakhtiari, J. CO<sub>2</sub> Methanation over NiO Catalysts Supported on CaO-Al<sub>2</sub>O<sub>3</sub>: Effect of CaO: Al<sub>2</sub>O<sub>3</sub> Molar Ratio and Nickel Loading. *Int. J. Hydrogen Energy* **2023**, *48* (98), 38664–38675.
- (26) Nobakht, A. R.; Rezaei, M.; Alavi, S. M.; Akbari, E.; Varbar, M. Synthesis and Evaluation of the Cobalt-Promoted NiO/CaO.2Al<sub>2</sub>O<sub>3</sub> Catalysts in CO<sub>2</sub> Methanation Reaction: Effect of Different Promoters. *J. CO<sub>2</sub> Util.* **2023**, *75*, 102577.
- (27) Valinejad Moghaddam, S.; Rezaei, M.; Meshkani, F.; Daroughegi, R. Carbon Dioxide Methanation over Ni-M/Al<sub>2</sub>O<sub>3</sub> (M: Fe, Co, Zr, La and Cu) Catalysts Synthesized Using the One-Pot Sol-Gel Synthesis Method. *Int. J. Hydrogen Energy* **2018**, *43* (34), 16522–16533.
- (28) Guilera, J.; Del Valle, J.; Alarcón, A.; Díaz, J. A.; Andreu, T. Metal-Oxide Promoted Ni/Al<sub>2</sub>O<sub>3</sub> as CO<sub>2</sub> Methanation Micro-Size Catalysts. *J. CO<sub>2</sub> Util.* **2019**, *30*, 11–17.
- (29) Rivero-Mendoza, D. E.; Stanley, J. N. G.; Scott, J.; Aguey-Zinsou, K. F. An Alumina-Supported Ni-La-Based Catalyst for Producing Synthetic Natural Gas. *Catalysts* **2016**, *6* (11), 1–15.
- (30) Battumur, N.; Sergelenbaatar, N.; Bold, T.; Byambajav, E. Cerium-Promoted Nickel Catalysts Supported on Yttrium-Doped  $\gamma$ -Alumina for Carbon Dioxide Methanation. *J. CO<sub>2</sub> Util.* **2023**, *68*, 102380.

- (31) Al-Fatesh, A. S.; Naeem, M. A.; Fakeeha, A. H.; Abasaheed, A. E. CO<sub>2</sub> Reforming of Methane to Produce Syngas over  $\gamma$ -Al<sub>2</sub>O<sub>3</sub>-Supported Ni–Sr Catalysts. *Bull. Chem. Soc. Jpn.* **2013**, *86* (6), 742–748.
- (32) Miccio, F.; Murri, A. N.; Landi, E. High-Temperature Capture of CO<sub>2</sub> by Strontium Oxide Sorbents. *Ind. Eng. Chem. Res.* **2016**, *55* (23), 6696–6707.
- (33) Nasreen, S.; Liu, H.; Khan, R.; Zhu, X.; Skala, D. Transesterification of Soybean Oil Catalyzed by Sr-Doped Cinder. *Energy Convers. Manage.* **2015**, *95*, 272–280.
- (34) Toemen, S. Effect of Strontium on the Catalytic Activity and Physicochemical Properties of Ru/Mn Catalysts for CO<sub>2</sub> Methanation Reaction. *AMR* **2015**, *1107* (3), 371–376.
- (35) Rhodes, N. R.; Barde, A.; Randhir, K.; Li, L.; Hahn, D. W.; Mei, R.; Klausner, J. F.; Auyeung, N. Solar Thermochemical Energy Storage Through Carbonation Cycles of SrCO<sub>3</sub>/SrO Supported on SrZrO<sub>3</sub>. *ChemSusChem* **2015**, *8* (22), 3793–3798.
- (36) Li, S.; Zhang, H.; Xu, J.; Yang, D. Hydrothermal Synthesis of Flower-like SrCO<sub>3</sub> Nanostructures. *Mater. Lett.* **2005**, *59* (4), 420–422.
- (37) Du, F.; Shi, L. Solvothermal Growth of Single-Crystal Hexagonal Prismatic SrCO<sub>3</sub> Microrods. *Cryst. Res. Technol.* **2007**, *42* (3), 216–220.
- (38) Van Doveren, H.; Verhoeven, J. A. T. H. XPS Spectra of Ca, Sr, Ba and Their Oxides. *J. Electron Spectrosc. Relat. Phenom.* **1980**, *21* (3), 265–273.
- (39) Mullins, W. M.; Averbach, B. L. Bias-reference X-Ray photoelectron spectroscopy of sapphire and yttrium aluminum garnet crystals. *Surf. Sci.* **1988**, *206*, 29–40.
- (40) Sinha, S.; Badrinarayanan, S.; Sinha, A. P. B. Interaction of Oxygen with Zr<sub>76</sub>Fe<sub>24</sub> Metglass: An X-Ray Photoelectron Spectroscopy Study. *J. Less-Common Met.* **1986**, *125*, 85–95.
- (41) Khatri, J.; Al-Fatesh, A. S.; Fakeeha, A. H.; Ibrahim, A. A.; Abasaheed, A. E.; Kasim, S. O.; Osman, A. I.; Patel, R.; Kumar, R. Ce Promoted Lanthana-Zirconia Supported Ni Catalyst System: A Ternary Redox System for Hydrogen Production. *Mol. Catal.* **2021**, *504*, 111498.
- (42) Li, G.; Li, W.; Zhang, M.; Tao, K. Characterization and Catalytic Application of Homogeneous Nano-Composite Oxides ZrO<sub>2</sub>–Al<sub>2</sub>O<sub>3</sub>. *Catal. Today* **2004**, *93–95*, 595–601.
- (43) Jin, S.; Dong, G.; Luo, J.; Ma, F.; Wang, C. Improved Photocatalytic NO Removal Activity of SrTiO<sub>3</sub> by Using SrCO<sub>3</sub> as a New Co-Catalyst. *Appl. Catal., B* **2018**, *227*, 24–34.
- (44) Ogo, S.; Onda, A.; Iwasa, Y.; Hara, K.; Fukuoka, A.; Yanagisawa, K. 1-Butanol Synthesis from Ethanol over Strontium Phosphate Hydroxyapatite Catalysts with Various Sr/P Ratios. *J. Catal.* **2012**, *296*, 24–30.
- (45) Lahuri, A. H.; Yarmo, M. A.; Tahari, M. N. A. Ultrasonic Assisted Synthesis of Bimetal Composite Strontium Oxide/Iron(III) Oxide for the Adsorption Isotherm Analysis of CO<sub>2</sub> Capture. In *Proceedings of the 3rd International Conference on Separation Technology*, Zaini, M. A. A.; Jusoh, M.; Othman, N., Eds.; Springer: Singapore, 2021; pp 175195
- (46) Al-Fatesh, A. S.; Kumar, R.; Kasim, S. O.; Ibrahim, A. A.; Fakeeha, A. H.; Abasaheed, A. E.; Atia, H.; Armbruster, U.; Kreyenschulte, C.; Lund, H.; Bartling, S.; Ahmed Mohammed, Y.; Albaqmaa, Y. A.; Lanre, M. S.; Chaudhary, M. L.; Almubaddel, F.; Chowdhury, B. Effect of Cerium Promoters on an MCM-41-Supported Nickel Catalyst in Dry Reforming of Methane. *Ind. Eng. Chem. Res.* **2022**, *61* (1), 164–174.
- (47) Zhao, Z.; Liu, L.; Zhang, X.; Tu, B.; Ou, D.; Cheng, M. Carbonates Formed during BSCF Preparation and Their Effects on Performance of SOFCs with BSCF Cathode. *Int. J. Hydrogen Energy* **2012**, *37* (24), 19036–19044.
- (48) Bai, G.; Li, F.; Fan, X.; Wang, Y.; Qiu, M.; Ma, Z.; Niu, L. Continuous Hydrogenation of Hydroquinone to 1,4-Cyclohexanediol over Alkaline Earth Metal Modified Nickel-Based Catalysts. *Catal. Commun.* **2012**, *17*, 126–130.
- (49) Kumar, R.; Shah, S.; Bahadur, J.; Melnichenko, Y. B.; Sen, D.; Mazumder, S.; Vinod, C. P.; Chowdhury, B. Highly Stable In-SBA-15 Catalyst for Vapor Phase Beckmann Rearrangement Reaction. *Microporous Mesoporous Mater.* **2016**, *234*, 293–302.
- (50) Bravo-Suárez, J. J.; Subramaniam, B.; Chaudhari, R. V. Vapor-Phase Methanol and Ethanol Coupling Reactions on CuMgAl Mixed Metal Oxides. *Appl. Catal., A* **2013**, *455* (2010), 234–246.